THE JOURNAL OF PHYSICAL CHEMISTRY C

pubs.acs.org/JPCC Article

Internal Atomic-Scale Structure Determination and Band Alignment of II–VI Quantum Dot Heterostructures

Cecilia M. Gentle, Yuanheng Wang, Tyler N. Haddock, Conner P. Dykstra, and Renske M. van der Veen*

Cite This: J. Phys. Chem. C 2020, 124, 3895–3904 Read Online

ACCESS | Metrics & More | Article Recommendations | Supporting Information

ABSTRACT: This work shows that ZnTe/CdSe core/shell quantum dots synthesized by a standard literature procedure in actuality have an alloyed $Cd_xZn_{1-x}Te$ core. We employ X-ray absorption spectroscopy (XAS) at all four K-shell ionization edges (Zn, Te, Cd, and Se) and perform global fitting analysis to extract the first-shell bond distances. We combine our XAS results with transmission electron microscopy (TEM) sizing and elemental analyses, which allows us to propose models of the internal particle structure. Our multimodal characterization approach confirms (1) the presence of Cd–Te bonds, (2) cation alloying in the particle core (and the absence of anion alloying), and (3) a patchy pure-phase CdSe shell. We synthesize particles of different shell thicknesses and performed synthetic control studies that allowed us to discard a ZnTe/CdTe/CdSe core/shell/shell structure and confirm the alloyed core/shell structure. Our structural analysis is extended with electronic band structure calculations and UV/vis absorption spectroscopy, demonstrating that the alloyed $Cd_xZn_{1-x}Te$/CdSe core/shell quantum dots exhibit a direct band gap, different from the predicted type II band alignment of the intended ZnTe/CdSe core/shell quantum dots. This study highlights the challenges with synthesizing II–VI quantum dot heterostructures and the power of XAS for understanding the internal structure of heterogeneous nanoparticles.

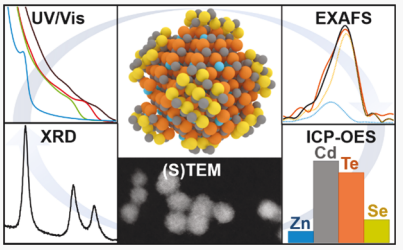

INTRODUCTION

Colloidal semiconductor nanocrystals, that is, quantum dots (QDs), exhibit size- and shape-dependent optoelectronic properties due to their quantum-confined (excited) states. Their tunability and synthetic flexibility make them ideal candidates for applications in solar energy harvesting, biomedical imaging, photocatalysis, light-emitting devices, and quantum computing.[1−3] Optical and electronic properties can be further tailored when two or more semiconducting materials are put together, forming a QD heterostructure.[4−9] Compared to pure-phase QDs, core/shell QDs (CSQDs) exhibit two additional degrees of freedom for tuning the energetics of the nanoparticle: the shell material and thickness. This can lead to two main types of band alignment: type I and type II. In type I heterostructures, the band gap of one material is encompassed within the band gap of the other material, which confines excited charge carriers (electrons and holes) exclusively within the material containing the smaller band gap. In type II structures, the band energies have a staggered band alignment that can result in separation of carriers across the material interface, benefitting charge extraction toward the electrodes in a photovoltaic device. Additional control over the spatial distribution patterns of charge carriers is achieved by varying the structure of the heterojunction itself, that is, making it epitaxial and sharp or alloyed and smooth. In fact, the wave function engineering approach in CSQDs[10,11] that makes use of epitaxial strain and alloying through ion exchange reactions has led to, for example, enhanced photoluminescence quantum yields,[5,6] reduced charge carrier recombination,[12,13] and their use as luminescent solar concentrators.[14,15]

Despite the myriad of synthetic and theoretical approaches that have recently been put forward to control the properties of heterostructured nanomaterials, their internal atomic-scale characterization remains challenging. Optical methods such as ultraviolet/visible (UV/vis) spectroscopy and photoluminescence (PL) are indispensable, but without much a priori knowledge about the heterostructure, the assignment of spectroscopic features can be ambiguous. Structural tools such as X-ray diffraction (XRD) provide information about the crystal symmetry and lattice spacing, but due to nanocrystal size broadening effects, structural subtleties such as strain and alloying remain hidden.[16] Angle-resolved X-ray photoelectron spectroscopy (XPS) was applied in the characterization of heterostructured nanomaterials,[16,17] but it has the drawback that the relatively small attenuation length of the photoelectrons limits the layer/shell thickness that can be studied. Recently, atom probe tomography (APT) has been used in the three-dimensional reconstruction of core/shell nanoparticles.[18−20] While this technique is powerful and promising, the sample preparation and experiment procedures for

Received: December 10, 2019
Revised: January 14, 2020
Published: January 15, 2020

https://dx.doi.org/10.1021/acs.jpcc.9b11443
J. Phys. Chem. C 2020, 124, 3895–3904

nanoparticles are challenging.[21] Finally, while high-resolution electron microscopy has been successfully applied in the characterization of heterostructured nanomaterials,[18,22−25] its use for core/shell QDs is limited due to their spherical symmetry, especially in the case of semiconducting materials with similar lattice spacing and/or similar atomic Z numbers. In this contribution, we make use of X-ray absorption spectroscopy (XAS) in the construction of atomic-scale structural models of CSQDs. XAS is ideally suited for probing the internal structure of multicomponent materials because of its elemental specificity and sensitivity to the local structure surrounding the absorbing atom.[26−33] In particular, the extended X-ray absorption fine structure (EXAFS) region of the XAS spectrum can ascertain coordination numbers, distinguish between types of scattering atoms, calculate bond lengths, and determine bond angles in the local (∼6 Å) environment of the absorbing atom in the nanoparticle.

We apply a multimodal approach based on UV/vis spectroscopy, transmission electron microscopy (TEM), elemental analysis, and XAS to determine the internal structure of intended II−VI ZnTe/CdSe core/shell nanoparticles. ZnTe/CdSe is a promising type II heterostructure due to the very small lattice mismatch between the ZnTe and CdSe zinc blende crystal structures (0.8%)[34] and the large conduction band offset, which enhances photovoltage,[35] minimizes overlap between electron and hole carriers,[36,37] and enables tunable emission in the near-IR.[34,38,39] The majority of previously reported synthetic procedures for colloidal ZnTe/CdSe CSQDs rely on the successive ion layer adsorption and reaction (SILAR) method.[34,35,38] In SILAR, the alternation of successive injections of elemental precursor solutions is used to control shell growth and avoid the formation of pure QD byproducts, ideally growing single monolayers of material per injection cycle. However, under reaction conditions that are prevalent in SILAR, that is, elevated temperatures and the presence of excess precursors, competing reactions such as ion exchange[40] and unintended precursor reactions and growth may occur. Here, we show that ZnTe/CdSe CSQDs synthesized according to the commonly employed SILAR method[34] are in actuality alloyed $Cd_xZn_{1-x}Te$/CdSe core/shell quantum dots. We studied the local structure of each elemental component of these complex nanoparticles by individually probing the Zn, Te, Cd, and Se X-ray absorption K-edges. By combining our XAS results with TEM sizing and elemental analyses, we propose models of the internal particle structure for a range of samples synthesized with different numbers of SILAR cycles. Our multimodal characterization approach confirms (1) the abundance of Cd−Te bonds, (2) cation alloying in the particle core (and the absence of anion alloying), (3) significant particle growth due to unreacted precursors, and (4) a patchy pure-phase CdSe shell. We extend our structural analysis with electronic band structure calculations and UV/vis absorption spectroscopy, demonstrating that the alloyed $Cd_xZn_{1-x}Te$/CdSe CSQDs behave as type I materials with a direct band gap, different from the predicted type II band alignment of the intended ZnTe/CdSe CSQDs. This study highlights the synthetic challenges associated with accessing colloidal type II II−VI heterostructures[40] and the power of XAS for understanding the internal structure of heterogeneous nanoparticles.

MATERIALS AND METHODS

Chemicals. Tellurium powder (99.8%, 200 mesh), cadmium oxide (CdO, 99.5%), selenium powder (99.5%, 100 mesh), oleic acid (OA, 90%), 1-octadecene (ODE, 90%), trioctylphosphine (TOP, 90%), hexadecylamine (HDA, 90%), diethylzinc ($ZnEt_2$, 1.0 M in hexanes), and toluene (ACS reagent, 99.5%) were purchased from Millipore Sigma.

Precursors. The 0.1 M cadmium precursor solution used for the CdSe shell growth was prepared by dissolving 0.1602 g of CdO in a mixture of 3.09 g of oleic acid and 9 mL of ODE at 240 °C under a nitrogen atmosphere. The 0.1 M selenium precursor solution was prepared by dissolving 0.1580 g of Se in 5 mL of TOP and 15 mL of ODE in a glove box. TOP-Te was prepared by dissolving 0.638 g of Te in 20 mL of TOP at ∼80 °C for 1 h in a glove box.

Synthesis of Core/Shell Nanoparticles. CSQDs were synthesized via the one-pot SILAR method.[34] Four QD samples were prepared using this method: SILAR 0.5, SILAR 1, SILAR 2, and SILAR 3. First, the 3.1 nm-diameter ZnTe cores were grown by quickly injecting a solution of 0.50 mmol of Te and 0.50 mmol of $Zn(Et)_2$ in 2 mL of trioctylphosphine into the reaction flask containing 3 g of hexadecylamine and 4 g of 1-octadecene at 300 °C and under a nitrogen atmosphere. Following injection, the reaction temperature was set to 270 °C to allow nanoparticles to grow for 3 min. The ZnTe core solution was then cooled to 240 °C and exposed to successive injections of Cd and Se precursor solutions. The SILAR 0.5 sample was prepared by adding 2.3 mL of a 0.1 M Cd-oleate solution dropwise to the ZnTe core solution, letting it react for 10 min, and quenching the reaction by removing the reaction flask from the heat and cooling the flask quickly with compressed air. No Se was added for this sample. In the case of the SILAR 1 sample, after 10 min of reaction with the Cd-oleate precursor, the same amount of Se precursor solution (0.1 M Se in TOP and ODE) was also added dropwise. After another 10 min, the reaction was quenched by removing the reaction flask from the heat and cooling the flask quickly with compressed air. Subsequent shell growth was done by repeating these SILAR cycles with a 10 min reaction time in between additions and increasing amounts of precursor to account for particle growth (2.9 mL for SILAR 2 and 3.6 mL for SILAR 3). After quenching, the nanocrystals were washed three times in toluene/acetone and suspended in 20 mL of toluene.

CdSe QDs (3.4 ± 0.3 nm) were prepared by a common hot-injection approach, as described by Yang et al.[41] The reaction flask was prepared by loading 60 mg of CdO, 2 g of oleic acid, and 14 mL of ODE into a three-necked flask under argon flow and stirred at 255 °C until CdO was completely dissolved. The selenium precursor was prepared in a glove box by dissolving 160 mg of Se powder in 2 mL of TOP and loaded into a syringe. The TOP-Se solution was then injected into the Cd precursor solution with rapid stirring and kept at 255 °C for 8 min, followed by cooling down to room temperature. The product was then washed with acetone and redispersed in 20 mL of toluene.

CdTe QDs (6.3 ± 0.5 nm) were prepared by the common hot-injection procedure of Dorfs et al.[42] The Cd-tetradecylphosphonic acid (TDPA) precursor was prepared by degassing 0.24 g of TDPA under nitrogen flow for 1 h at 100 °C, followed by dissolution of 0.033 g of CdO under a nitrogen atmosphere between 250 and 300 °C until the mixture became

https://dx.doi.org/10.1021/acs.jpcc.9b11443
J. Phys. Chem. C 2020, 124, 3895−3904

clear. TOP-Te was prepared by dissolving 0.19 g of Te in 10 mL of TOP at ~80 °C for 1 h under a nitrogen atmosphere. The Cd-TDPA precursor, 0.22 g of HDA, and 7.8 mL of ODE were degassed under nitrogen flow for 1 h at 100 °C. The temperature was then raised to 280 °C, and 2 mL of the TOP-Te precursor is subsequently injected. After the injection, the temperature of the mixture is reduced and maintained at 260 °C for the growth of nanocrystals. The reaction was stopped by temperature quenching with a water bath. The product obtained was purified using toluene as the solvent and an isopropanol/methanol mixture as the nonsolvent. The final purified product was suspended in 10 mL of toluene.

UV/Visible Spectroscopy, PL, XRD, TEM, and Elemental Analysis. UV/vis absorption spectroscopy was performed using a Varian CARY 5G spectrophotometer. PL quantum yields were determined using an integrating sphere. The PL spectra were collected with a Horiba Jobin Yvon FluoroMax-3 fluorometer (excitation wavelength, 532 nm), and decay curves were obtained by time-correlated single-photon counting (excitation wavelength, 532 nm; 120 ps pulse width; 3.13 MHz repetition rate; 200 $\mu J/cm^2$). Powder XRD patterns were obtained by a Bruker D8 ADVANCE diffractometer with a Mo-Kα radiation source and a LYNXEYE XE detector. TEM measurements were performed using a JEOL 2100 Cryo TEM operating at 200 kV acceleration voltage. The samples for electron microscopy were prepared by drop-casting a suspension (typically 10 μL of 100× diluted as-synthesized sample) on a holey carbon film supported by a copper TEM grid. TEM grids with ZnTe QDs were prepared inside a glove box and transferred inside the TEM as rapid as possible (~1 min). On the basis of the TEM images, size histograms, mean diameters, and size dispersions of the QDs are determined by analyzing 100−200 particles for each sample. High annular dark-field (HAADF) scanning TEM (STEM) and high-resolution TEM (HRTEM) images were taken using a FEI Themis Z advanced probe aberration-corrected analytical transmission electron microscope/scanning transmission electron microscope. Samples were evaluated for Zn, Te, Cd, and Se composition using a Perkin Elmer Optima 8300 inductively coupled plasma-optical emission spectrophotometer.

X-ray Absorption Spectroscopy. XAS experiments were performed at the 9 BM and 20 BM beam lines at the Advanced Photon Source (APS), Argonne National Laboratory. One milliliter of sample (~800 nM particle concentration that corresponds to elemental concentrations of 2 mM Se and 4 mM Zn in toluene) was loaded into a custom-made Teflon liquid sample cell. A 2.5 μm-thin Mylar sheet was used to seal the sample cell. An ion chamber detector was used to monitor the X-ray intensity before the sample. Signal collection was done in partial fluorescence mode with a Canberra 13-element Ge detector. The monochromator energies were calibrated by measuring the spectra of a Zn, Se, and Sb (for the Cd and Te K-edges) foil in transmission.[43]

The X-ray spectra were analyzed using the FEFF-based Athena and Artemis EXAFS fitting packages,[44] including background subtraction, normalization, energy calibration, and single-shell Fourier analysis. Bulk zinc blende ZnTe, CdTe, and CdSe crystal structures[45] were used as an input from which bond distances were refined. In our analysis, we simultaneously fit the first single-scattering shells at all four absorption edges (Zn, Cd, Te, and Se) of the same sample. The amplitude reduction factors, S_0^2, were obtained from separate EXAFS data on CdSe and CdTe QDs and a Zn foil. They were then held fixed in the fits of the CSQD data. The energy shift ΔE_0 and coordination numbers N were fit for each absorption edge separately. As a constraint, we used the same mean change in bond length ΔR and mean-square displacement factor σ^2 for identical bonds at different edges (e.g., Zn−Te at the Zn edge and Te−Zn at the Te edge). In this way, we were able to reduce the total number of free fitting parameters to 16, which is significantly less than the number of independent data points (47, see Supporting Information section 6 for details). Data were fit in R-space and k-space simultaneously, and the k-space EXAFS spectra were weighted with k, k^2, and k^3 to alleviate the correlation between parameters. The fitting data ranges are given in Supporting Information section 6.

RESULTS AND DISCUSSION

Nanoparticle Characterization by UV/vis, XRD, and TEM. Figure 1a shows the results from UV/vis spectroscopy

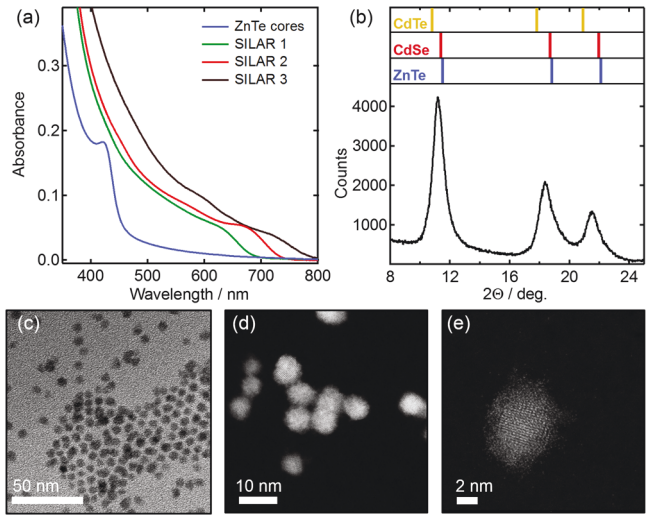

Figure 1. (a) UV/vis spectra of 3.1 ± 0.5 nm ZnTe cores (blue), 5.0 ± 0.8 nm CSQDs after one SILAR cycle (SILAR 1, green), 5.7 ± 0.7 nm CSQDs after two SILAR cycles (SILAR 2, red), and 6.6 ± 0.6 nm CSQDs after three SILAR cycles (SILAR 3, black). (b) Powder XRD pattern of SILAR 2 CSQDs. The top of the plot shows line spectra for bulk zinc blende ZnTe (blue), CdSe (red), and CdTe (yellow). (c) TEM and (d, e) HAADF-STEM images of 5.7 ± 0.7 nm SILAR 2 CSQDs. All particle sizes were determined by TEM using a sample size of 100−200 particles.

on the ZnTe cores, and the SILAR 1, SILAR 2, and SILAR 3 samples. As the number of SILAR cycles increases and the particles grow, a clear red shift and decrease in the first exciton intensity are observed. This behavior is typically interpreted as the appearance of a spatially indirect transition, that is, a charge transfer state across the interface between the two semiconductors, which extends the absorption of type II CSQDs to longer wavelengths and reduces the electron−hole wave function overlap.[34,38,46,47] As discussed below, however, the red shift can also be caused by alloying. The XRD (Figure 1b) and (S)TEM data (Figure 1c−e, see Supporting Information sections 2−4 for more images) show that the CSQDs are highly crystalline, but a detailed atomic-scale structural analysis is precluded due to size broadening of the diffraction peaks and the absence of intraparticle contrast variations in the STEM

https://dx.doi.org/10.1021/acs.jpcc.9b11443
J. Phys. Chem. C 2020, 124, 3895−3904

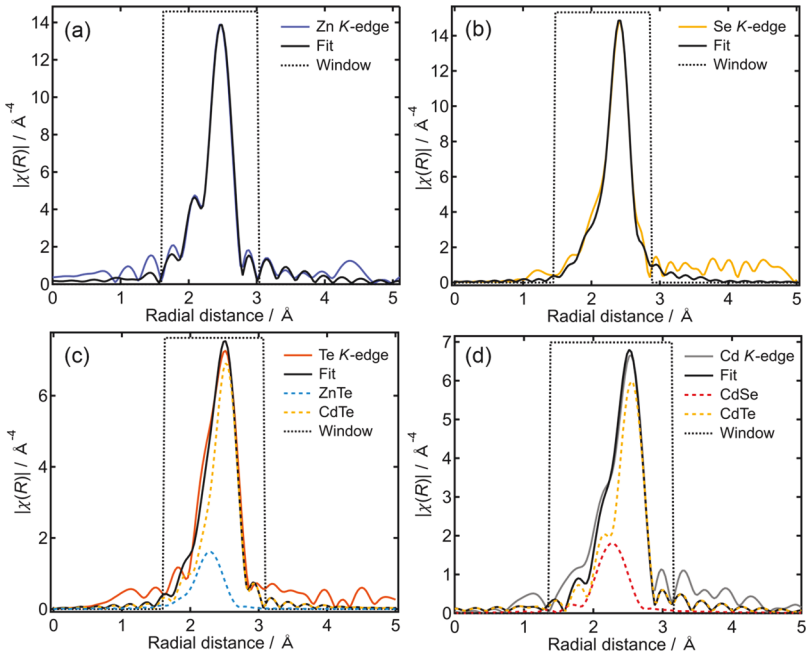

Figure 2. Fourier-transformed EXAFS data of SILAR 2 CSQDs. (a) Zn K-edge data (blue) and fit to the ZnTe zinc blende structure (black). (b) Se K-edge data (yellow) and fit to the CdSe zinc blende structure (black). (c) Te K-edge data (dark orange), fit to the ZnTe and CdTe zinc blende structures (black), and individual first-shell contributions of ZnTe (20%, blue) and CdTe (80%, yellow). (d) Cd K-edge data (gray), fit to the CdSe and CdTe zinc blende structures (black), and individual first-shell contributions of CdSe (22%, red) and CdTe (78%, yellow). The *k*-space EXAFS data $\chi(k)$ were weighted by k^3 before Fourier transformation, and the *R*-space axes are not phase-corrected. The fitting ranges in *R*-space are shown as dashed black window functions in each graph.

images. Energy dispersive spectroscopy (EDS) STEM was attempted, but due to substantial electron beam-induced sample damage, it could not be used to obtain element-specific information about the particle structure. Based on the above information, it is clear that "conventional" materials characterization tools cannot be used to unambiguously determine the internal atomic-scale nanoparticle structure. We therefore used X-ray spectroscopy as an element-specific and structurally sensitive probe.

First-Shell Global Fit Analysis of X-ray Absorption Fine Structure. We measured the XAS spectra at the K-edges of all four elements (Zn, Se, Te, and Cd) in the CSQD nanoparticles of the SILAR 2 sample. We focus our analysis on the EXAFS spectra ~100−1600 eV above the ionization edges. The absorption cross-section modulations in this spectral region can phenomenologically be interpreted as resulting from the interference of outgoing and backscattered photoelectron waves emanating from the X-ray absorbing atom. As such, the EXAFS spectrum is particularly sensitive to the local structure (bond lengths and symmetry) and coordination numbers. We extracted the EXAFS by normalization and background subtraction (see Materials and Methods and Supporting Information section 5), after which the fine structure is multiplied by k^n (n = 1−3) and Fourier-transformed to yield the effective radial distribution function (RDF), that is, the distribution of distances between the absorbing atom and surrounding atoms in a sphere of ~6 Å (besides a constant phase shift that can be calculated[48]). The effective RDFs, as shown in Figure 2, exhibit only one dominant peak at each absorption edge, which indicates that, in these materials, EXAFS is only sensitive to the nearest-neighbor cation−anion distances. The whole set of EXAFS data was therefore analyzed with a first-shell Fourier approach with the bond length change ΔR, mean-square disorder parameter σ^2 (describing thermal and static disorder), coordination number N, and ionization energy E_0 as fitting parameters (see Materials and Methods for details).

EXAFS analysis is prone to overfitting due to the large number of fitting parameters necessary for each coordination shell and the overlap of single- and multiple-scattering pathways due to similar bond distances in the vicinity of the absorbing atom. To reduce the number of fitting parameters, we measured the EXAFS spectra on pure-phase CdSe and CdTe QDs and used the fitted amplitude reduction factors S_0^2 at the Cd, Se, and Te edges as fixed parameters in the EXAFS fits of the CSQDs. Due to facile oxidation, we did not measure the EXAFS of pure-phase ZnTe QDs. Instead, we use the S_0^2 parameter obtained from EXAFS fitting of a Zn foil. We further reduced the number of parameters significantly by performing a global fit of all four EXAFS data sets simultaneously and by using the same ΔR and σ^2 parameters at different ionization edges (e.g., the Zn−Te bond length change and mean-square disorder parameter are identical at the Zn and Te edges).

We tested two models by globally fitting the four data sets in Figure 2. In the first model, each RDF is fit to a pure-phase zinc blende structure, that is, ZnTe at the Zn and Te edges and CdSe at the Cd and Se edges. This case applies for ZnTe/CdSe core/shell QDs with a relatively sharp interface (negligible alloying). As shown in Supporting Information section 7, this model did not yield satisfactory fit results. The second model includes the CdTe zinc blende structure in the fit at the Cd and Te edges, the relative stoichiometric contribution of which is fit using weight parameters x (Cd edge) and y (Te edge) ($0 \leq x,y \leq 1$) as global fitting parameters. The resulting fits were significantly improved and show excellent agreement with the data, as shown in Figure 2

https://dx.doi.org/10.1021/acs.jpcc.9b11443
J. Phys. Chem. C 2020, 124, 3895−3904

Table 1. EXAFS Fitting Results at the Zn, Se, Te, and Cd K-Edges[a]

bond	ΔR (Å)	R_{Bulk} (Å)[28]	σ^2 (Å^2)	weight
CSQDs (SILAR 2)				
Zn−Te	0.009 ± 0.006	2.643	0.0065 ± 0.0007	
Se−Cd	−0.011 ± 0.005	2.631	0.0057 ± 0.0006	
Te−Zn	0.009 ± 0.006	2.643	0.0065 ± 0.0007	0.20 ± 0.07 $(1 - y)$
Te−Cd	−0.019 ± 0.005	2.806	0.0064 ± 0.0006	0.80 ± 0.07 (y)
Cd−Se	−0.011 ± 0.005	2.631	0.0057 ± 0.0006	0.22 ± 0.04 $(1 - x)$
Cd−Te	−0.019 ± 0.005	2.806	0.0064 ± 0.0006	0.78 ± 0.04 (x)
CdTe QDs (6.3 ± 0.5 nm)				
Te−Cd	−0.012 ± 0.003	2.806	0.0069 ± 0.0003	
Cd−Te	−0.012 ± 0.003	2.806	0.0069 ± 0.0003	
CdSe QDs (3.4 ± 0.3 nm)				
Se−Cd	−0.020 ± 0.005	2.631	0.0058 ± 0.0005	
Cd−Se	−0.020 ± 0.005	2.631	0.0058 ± 0.0005	

[a]ΔR is the bond length change relative to the bulk (R_{Bulk}), σ^2 is the mean-square disorder of neighboring distances (Debye−Waller parameter), x is the fraction of Cd−Te bonds at the Cd edge, and y is the fraction of Cd−Te bonds at the Te edge. All four data sets for the CSQDs were fit simultaneously, and the ΔR and σ^2 parameters for the same bonds were set to be equal. The X-ray-absorbing atom is denoted in bold typeface and written first.

(see Supporting Information sections 6 and 7 for a comparison of the fit statistics). We note that the Zn and Se edge data can be perfectly fit with pure-phase ZnTe and CdSe structures, respectively.

Table 1 summarizes the EXAFS fitting results for the SILAR 2 CSQD sample, as well as for pure-phase CdTe and CdSe QDs (see Supporting Information sections 6 and 7 for more fitting results). The fitted changes in first-shell bond lengths ΔR indicate a slight expansion of the Zn−Te bonds and a contraction of the Cd−Te bonds compared to the bulk and nanophase bond lengths. This indicates alloying of, and/or epitaxial strain between, the ZnTe and CdTe zinc blende structures, which have very different lattice parameters.[45] The Cd−Se bonds in the CSQDs are contracted with respect to the bulk but expanded compared to CdSe QDs. Since we expect CdSe to cover the surface of the CSQDs, the effects of strain and ligands on the Cd−Se bonds are hard to predict and no conclusions can be drawn. The fact that the mean-square disorder parameters σ^2 are all similar, regardless of the sample, evidences that the static disorder in the CSQDs is not larger than in pure-phase QDs. The weight parameters x and y are globally fit to $x = 0.78 \pm 0.04$ (Cd−Te contribution at the Cd edge) and $y = 0.80 \pm 0.07$ (Cd−Te contribution at the Te edge), which are in excellent agreement with results from inductively coupled plasma-optical emission spectrophotometry (ICP-OES) (see Supporting Information section 8).

EXAFS global fit analysis clearly shows that the CSQD particles do not exhibit a simple ZnTe/CdSe core/shell structure. Instead, they contain a significant fraction of Cd−Te bonds. The exact nature of the Cd−Te bonds, whether they are contained in a pure-phase CdTe intermediate shell or as a $Cd_xZn_{1-x}Te$ alloy, cannot be ascertained from the data since our Fourier analysis is restricted to the first shell only. In fact, it is well known that bond distances in substitutional ternary alloys derived from EXAFS are much closer to pure-phase bond lengths than those that could be derived using Vegard's law and XRD data.[49] On the other hand, the fact that the Zn and Se edge data can be perfectly described with pure-phase ZnTe and CdSe zinc blende structures, respectively, without the need to include much shorter Zn−Se bonds (2.42 Å in the bulk[45]), evidently shows that no anion alloying of the ZnTe core or cation alloying of the CdSe shell takes place. Therefore, within our experimental uncertainties, we can exclude the presence of $ZnTe_xSe_{1-x}$, $Cd_xZn_{1-x}Se$ or a homogeneous alloy $Cd_xZn_yTe_zSe_{x+y-z}$.

Particle Models and Control Experiments. Based on the EXAFS analysis, we propose two candidate particle heterostructure models: (I) core/shell/shell ZnTe/CdTe/CdSe and (II) alloyed core/shell $Cd_xZn_{1-x}Te$/CdSe. For simplicity, we assume that the nanoparticles are perfectly spherical and that the interfaces between the core and shells are sharp. For each SILAR sample, we determined the particle diameters and elemental ratios, as summarized in Figure 3 and Table S1. The number of atoms in the particle core or shell(s) can then be expressed as a function of the radii and the lattice constants (see Supporting Information section 9 for equations). Since the particle outer radius is determined by TEM sizing and the Te/Zn and Cd/Se elemental ratios are obtained from elemental analysis, we can determine the nanoparticle inner radii, that is, the core radius and interlayer thickness for model I and the alloyed core radius for model II, that best fit the data. The results are schematically shown in Figure 4a for the SILAR 2 sample.

We first note that the SILAR 0.5 sample, which is synthesized by exposing ZnTe cores to the Cd precursor only (no Se addition), already contains a significant amount of Cd−Te bonds either in the form of a pure-phase shell (model I) or incorporated in a $Cd_xZn_{1-x}Te$ alloy (model II). In fact, the nanoparticle diameter increases from 3.1 ± 0.5 nm for the ZnTe seeds to 4.3 ± 0.5 nm for the SILAR 0.5 sample, which indicates that the Cd not just adsorbs onto, or diffuses into, the ZnTe cores but rather new bonds are formed due to the unintended reaction of Cd and Te precursors. The latter are still in the solution since the ZnTe core synthesis is not quantitative, as is confirmed by a control experiment showing that ZnTe seeds continue to grow until 20 min after precursor injection at 240 °C (see Supporting Information section 10). It is noted, however, that previously reported synthesis procedures, which are similar to ours, do assume that the ZnTe seed formation is quantitative.[34,35,37,38,46] Interestingly, the UV/vis absorption also significantly shifts to longer wavelengths upon addition of the Cd precursor only (Figure 5), an effect that could either be interpreted as the formation

https://dx.doi.org/10.1021/acs.jpcc.9b11443
J. Phys. Chem. C 2020, 124, 3895−3904

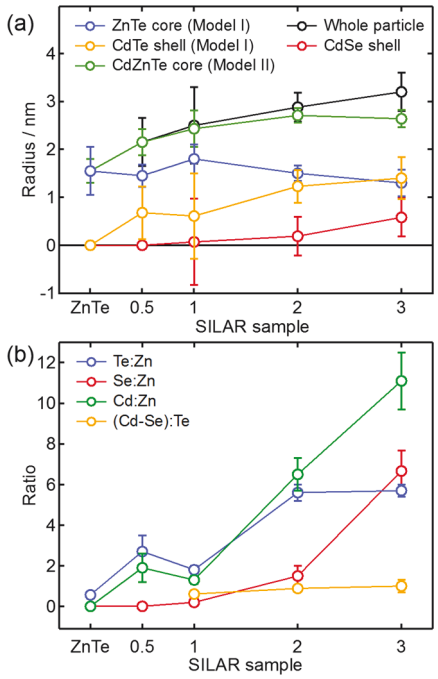

Figure 3. Results from TEM and elemental analysis. (a) Nanoparticle radii ratios for the ZnTe seeds and SILAR 0.5, 1, 2, and 3 samples. In the case of model I, the radii of the pure-phase ZnTe core and CdTe intermediate shell are plotted. In the case of model II, the radius of the alloyed CdZnTe core is plotted. The CdSe shell radius applies to both models. Error bars on the black line originate from TEM sizing, and error bars on the red and blue lines are propagated errors using a Monte Carlo procedure described in Supporting Information section 9. (b) Elemental ratios for the ZnTe seeds and SILAR 0.5, 1, 2, and 3 samples. The abscissae are proportional to time (from 0 for ZnTe to 60 min for SILAR 3). All error bars represent ±std. dev.

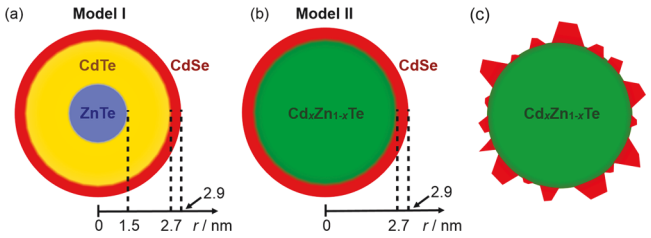

Figure 4. Nanoparticle models obtained from EXAFS, TEM, and elemental analysis. (a) Core/shell/shell ZnTe/CdTe/CdSe model I for the SILAR 2 sample. (b) Alloyed core/shell $Cd_xZn_{1-x}Te$/CdSe model II for the SILAR 2 sample ($x = 0.8 \pm 0.1$). The CdSe shell thickness is exaggerated and not to scale. In addition, the CdSe shell is shown to be uniform, which is not in agreement with TEM and EXAFS data. Instead, the CdSe shell is patchy, as schematically shown in (c).

of a (quasi-)type II heterostructure (e.g., ZnTe/CdTe) or the formation of a $Cd_xZn_{1-x}Te$ alloy.

Zn^{2+} for Cd^{2+} cation exchange is expected to play a major role under the present reaction conditions (240 °C, 3−60 min), as demonstrated in a recent study on ZnTe nanorods by Enright et al.[40] The core/shell/shell model I with sharp interfaces is therefore highly unlikely. In fact, this model predicts a slight decrease in the ZnTe core size as a function of SILAR cycle (Figure 3a), which is unrealistic given that the pure-phase CdTe shell would inhibit Zn^{2+} ion diffusion out of the core without the concomitant formation of an alloy across

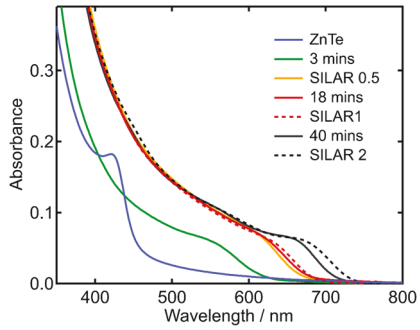

Figure 5. UV/vis spectra of pure-phase ZnTe cores (270 °C) and ZnTe cores that were cooled down to 240 °C and then exposed to 2.3 mL of a 0.1 M Cd-oleate solution. Aliquots were taken at 3, 10 (SILAR 0.5), and 18 min after the first Cd-oleate injection. An additional 2.9 mL of Cd precursor solution was added after 20 min, and an aliquot was taken after a total of 40 min to simulate the conditions of the SILAR 2 synthesis (but without Se addition). SILAR 1 and 2 data are also shown for comparison.

the ZnTe/CdTe interface. We therefore propose model II to be the most realistic model for heterostructures synthesized according to the SILAR procedures reported in the literature.[34,35,37,38,46]

The cation exchange reaction is expected to occur via a kick-out mechanism with a relatively small activation barrier of 24 kJ/mol,[5,50] where Cd^{2+} ions or [Cd−Te] monomers first saturate the ZnTe surface before they diffuse into the lattice through unoccupied tetrahedral interstitial sites.[51] Zn^{2+} ions can diffuse through interstitial sites outward before they readily combine with either HDA or oleate ions in solution.[39] In the present case, however, cation exchange coincides with the formation of new Cd−Te bonds through the reaction of Cd and Te precursors. The relatively small loss of Zn atoms inside the QDs over the course of the SILAR 0.5−3 reactions, as shown by the only slight decrease in ZnTe core size in model I (Figure 3a) and the rather constant (Cd−Se)/Te ratio (Figure 3b), indicates that the rate of CdTe formation is higher than, or at least comparable to, the rate of Zn^{2+} ion diffusion out of the lattice. The particles during the early SILAR cycles (0.5−1) may therefore be better described as a gradient alloy, with a Zn-rich core and a Cd-rich shell; their growth can be entirely attributed to the formation of new Cd−Te bonds. Indeed, hardly any CdSe is present for the SILAR 1 sample, which agrees with the lack of Se incorporation in the studies on ZnTe nanorods by Enright et al.[40] and the higher reactivity of elemental Te than elemental Se toward Cd.[52] During later SILAR cycles (2 and 3), particle growth is largely due to the formation of a CdSe shell (Figure 3a). Cation diffusion simulations (Supporting Information section 11) show that a nearly homogeneous $Cd_xZn_{1-x}Te$ core is formed on the timescales of SILAR cycles 2 and 3. A similar ion diffusion study based on the annealing of ZnTe/CdSe QDs at 250 °C[37] proposed the concomitant formation of a $Cd_xZn_{1-x}Se$ alloy, which can be clearly discarded on the basis of our EXAFS results (vide supra).

To investigate the role of TOP-Se, a synthesis was performed in the absence of Se precursors while keeping the Cd addition rates and other reaction conditions unchanged. Aliquots were taken at 3, 5, 10 (SILAR 0.5), 18, and 40 min to record the UV/vis spectra, as shown in Figure 5, together with the spectra of the SILAR 1 and 2 samples. The absorption onset continuously shifts to longer wavelengths, which is

https://dx.doi.org/10.1021/acs.jpcc.9b11443
J. Phys. Chem. C 2020, 124, 3895−3904

attributed to CdTe addition and alloying during SILAR cycles 0.5 and 1 and due to alloying and CdSe shell growth during SILAR cycles 2 and 3. By comparing the spectra at 18 and 40 min for the Cd-only reaction with the SILAR 1 and 2 spectra, it is seen that the CdSe shell influences the spectrum only minimally and the absorption onsets remain relatively abrupt. As we will show below, this behavior indicates a direct band gap transition (as opposed to a spatially indirect type II transition).

The particle models based on TEM sizing and elemental analysis assume that CdSe is added uniformly to the $Cd_xZn_{1-x}Te$ core. Under this assumption, the CdSe shell is only half a monolayer (ML) for the SILAR 2 sample and 2 ML for the SILAR 3 sample (1 ML ≈ 0.3 nm). Such extremely thin epitaxial shells would be subject to a significant degree of strain due to the relatively large lattice mismatch of 5−6%[45] between CdTe (or alloyed $Cd_{0.8}Zn_{0.2}Te$) and CdSe. Such effects are not seen in the EXAFS data at the Se K-edge; that is, the latter can be perfectly fit with the CdSe zinc blende structure with only minor (0.4%) deviations from the bulk structure (Table 1). Based on these results, we propose the presence of pure-phase CdSe islands on the alloyed CdZnTe core, which would minimize the interfacial strain (Figure 4c). In fact, Jiang and Kelley have indirectly derived that the CdSe shell must be rough by measuring the inhomogeneity in interfacial hole transfer rates to an adsorbed hole acceptor.[37,46] They concluded that CdSe shell formation proceeds via a Stranski−Krastanov growth mechanism at moderate temperatures with the formation of a uniformly strained film (the wetting layer) up to the critical thickness of several MLs, followed by the growth of three-dimensional islands on top of the uniform film. Our EXAFS results clearly disagree with the presence of a uniform, strained CdSe layer, especially since the amount of deposited CdSe is only minimal (Figure 4b). We therefore conclude that, under the present SILAR synthesis conditions, CdSe island growth occurs via the Volmer−Weber mechanism, which is dominant for interfaces with large lattice mismatch where the energetic cost of lattice strain exceeds that of the increased surface area associated with the islands.[37,53] The roughness of the CdSe shell is corroborated by the "patchiness" of the HAADF-STEM images of the SILAR 2 sample (Figure 1d,e). We also note that we can exclude the occurrence of an anion alloy $CdTe_xSe_{1-x}$ on the basis of a control experiment in which purified CdTe QDs are exposed to the TOP-Se precursor at 240 °C for 40 min. No changes in the UV/vis spectrum and ICP-OES were observed (see Supporting Information section 12), which is in agreement with the high activation barrier for anion exchange in similar systems.[22,51]

Wave Function Engineering Approach for Band Alignment and Wave Function Overlap. With the internal structure of the CSQDs determined as $Cd_xZn_{1-x}Te$/CdSe using EXAFS, TEM, and elemental analysis, we then applied a simple wave function engineering approach[54] (see Supporting Information section 13 for details) to determine the band alignment regime and electron−hole wave function overlap for the lowest-energy $1S_{hh}$ and $1S_e$ states. In this method, an effective mass approximation was made to simplify the atomic-scale variation of potentials. The hole and electron were assumed to move freely in averaged valence band and conduction band potentials, respectively, with certain effective masses (see Table S3 in Supporting Information section 13). As a result, both charge carriers can be treated by a simple particle-in-a-sphere model. The Schrödinger equations of both particles were solved using the finite difference method. Mean field approximation was applied to account for the Coulomb interaction between the electron and the hole (exciton binding energy), meaning that the electron moves in a mean potential induced by the hole Φ_h and the hole moves in a mean potential of the electron Φ_e. These potentials cannot be determined beforehand but can be calculated by Poisson equations if the electron and hole wave functions were known. As a result, a self-consistent computation of wave functions and band energies was applied.

To understand the influence of alloying on the band alignment, we performed calculations for both the core/shell/shell model I and the alloyed core/shell model II using the particle radii for the SILAR 2 sample (Figure 6). For simplicity,

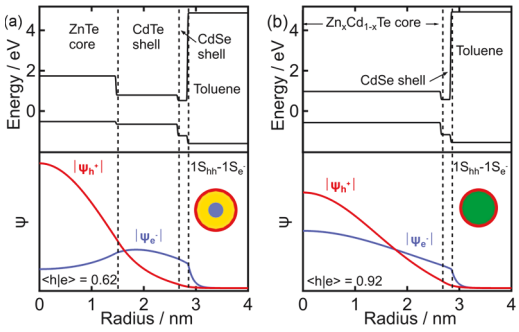

Figure 6. Band alignment calculations and wave function overlap. Top: The stair-shaped black lines show the confinement potentials of the valence and conduction bands (bulk values[45]). Bottom: The electron (blue) and hole (red) wave functions (Ψ) in the $1S_{hh}$ and $1S_e$ states for (a) the ZnTe/CdTe/CdSe core/shell/shell model I and (b) the alloyed $Cd_xZn_{1-x}Te$ core/CdSe shell model II. The radii for the cores and shells are those obtained from combining the TEM and elemental analysis results for the SILAR 2 sample ($x = 0.8 \pm 0.1$). The surrounding solvent is toluene. ⟨h|e⟩ denotes the electron−hole wave function overlap.

we neglect the fact that CdSe is present in the form of islands instead of a uniform layer, which does not significantly affect the conclusions drawn herein. While model I nanoparticles retain a quasi-type II band alignment for which the hole wave function spreads over the ZnTe/CdTe core/shell portion and the electron localizes inside the CdTe shell, resulting in a $1S_e-1S_{hh}$ electron−hole overlap of ∼0.6, the alloyed core model II nanoparticles act as a single-composition material with a much larger $1S_e-1S_{hh}$ electron−hole overlap of ∼0.9, similar to type I CSQDs.[55] The electron−hole wave function overlap is related to the oscillator strength in the UV/vis absorption spectrum. Since we see a rather pronounced $1S_e-1S_h$ exciton transition for all samples, except maybe SILAR 3 for which there is a weak low-energy tail, this indicates a direct band gap transition, as opposed to a spatially indirect lowest-energy band gap transition for a type II alignment. The thin CdSe shell of 0.2 nm has expectedly only a minimal influence on the wave function overlap, which is confirmed by the relatively small red shift of the first-exciton absorption onset in the UV/vis spectra upon CdSe incorporation (Figure 5). Our simulations (see Supporting Information section 14) indicate that a CdSe shell thickness of 1.36 nm is necessary to achieve a type II alignment and a $1S_e-1S_h$ electron−hole overlap of ∼0.5 for the $Cd_xZn_{1-x}Te$/CdSe CSQDs ($x = 0.8 \pm 0.1$, SILAR 2). In Supporting Information section 14, we show that gradient

https://dx.doi.org/10.1021/acs.jpcc.9b11443
J. Phys. Chem. C 2020, 124, 3895−3904

alloying of the core instead of homogeneously alloying only marginally changes the band alignment, wave function overlap, and calculated transition energies.

The large electron−hole wave function overlap for the $Cd_xZn_{1-x}Te$/CdSe CSQDs raises the question about their emission properties. We measured the PL yield and decay time and obtained <0.1% and ∼10 ± 0.1 ns (mean decay time, see Supporting Information section 1) for the SILAR 2 sample, respectively. These values show that the electron−hole recombination is dominated by nonradiative decay channels such as surface trap states. For the SILAR 2 sample, the latter could be dominant since the CdSe coverage is only small and the $Cd_xZn_{1-x}Te$ alloyed core, and therefore hole density, is expected to be largely exposed to the solvent. The SILAR 3 sample has a mean decay time of ∼76 ± 0.8 ns, which might be prolonged relative to the SILAR 2 sample due to a more complete coverage of the surface with CdSe, shielding the hole density away from the surface/solvent, as well as due to a slightly reduced electron−hole wave function overlap in this sample (type II behavior).

CONCLUSIONS

We have determined the internal structure of II−VI CSQDs using a multimodal characterization approach based on UV/vis, TEM, elemental analysis, and XAS. We show that the intended ZnTe/CdSe CSQDs, which are synthesized using a common one-pot SILAR procedure, are in actuality nanoparticles with an alloyed $Cd_xZn_{1-x}Te$ core and a patchy CdSe shell that essentially behave as one-component QDs with a direct band gap. Cation exchange and the unintended reaction of molecular precursors prevent the formation of a sharp type II ZnTe/CdSe interface with small lattice mismatch. Instead, the large interfacial strain between $Cd_xZn_{1-x}Te$ ($x \approx 0.8$) and pure-phase CdSe leads to the growth of islands on the QD surface. Our results corroborate the challenges associated with the synthesis of Zn/Cd chalcogenide type II heterostructures due to facile ion exchange, as pointed out previously by Enright et al.[40] and Groeneveld et al.[39] We note that the assessment of CSQDs on the basis of UV/vis and TEM analysis alone is not sufficient since alloy formation and particle growth due to unintended precursor reactions can cause similar trends, as expected for the formation of type II heterostructures. Here, we employ EXAFS spectroscopy as an element-specific technique for the internal structure determination of heterostructured nanomaterials. By simultaneously fitting the local atomic structures at the ionization edges of all four elements in the sample, we were able to propose models for the internal nanoparticle structure that were further scrutinized by TEM and elemental analysis. While our XAS data were obtained at a large-scale synchrotron X-ray facility with specialized infrastructure and limited access, the advent of tunable high-brightness table-top X-ray sources will enable similar studies on heterostructured photovoltaic and photocatalytic nanomaterials with a much higher throughput and more experimental flexibility.[56]

ASSOCIATED CONTENT

Supporting Information

The Supporting Information is available free of charge at https://pubs.acs.org/doi/10.1021/acs.jpcc.9b11443.

UV/vis, photoluminescence, TEM/STEM images, EXAFS fitting, nanoparticle structure models, synthetic control experiments, and band structure simulation (PDF)

AUTHOR INFORMATION

Corresponding Author

Renske M. van der Veen − *Department of Chemistry and Materials Research Laboratory, University of Illinois at Urbana−Champaign, Champaign, Illinois 61820, United States*; Email: renske@illinois.edu

Authors

Cecilia M. Gentle − *Department of Chemistry and Materials Research Laboratory, University of Illinois at Urbana−Champaign, Champaign, Illinois 61820, United States*; orcid.org/0000-0002-5364-3830

Yuanheng Wang − *Department of Chemistry and Materials Research Laboratory, University of Illinois at Urbana−Champaign, Champaign, Illinois 61820, United States*

Tyler N. Haddock − *Department of Chemistry and Materials Research Laboratory, University of Illinois at Urbana−Champaign, Champaign, Illinois 61820, United States*

Conner P. Dykstra − *Department of Chemistry and Materials Research Laboratory, University of Illinois at Urbana−Champaign, Champaign, Illinois 61820, United States*

Complete contact information is available at: https://pubs.acs.org/10.1021/acs.jpcc.9b11443

Author Contributions

The manuscript was written through contributions of all authors. All authors have given approval to the final version of the manuscript.

Notes

The authors declare no competing financial interest.

ACKNOWLEDGMENTS

The UV/vis absorption spectroscopy and (S)TEM experiments were carried out in the Materials Research Laboratory Central Facilities at the University of Illinois at Urbana−Champaign (UIUC). ICP-OES measurements were carried out by the Microanalysis Laboratory in the School of Chemical Sciences at UIUC. We gratefully acknowledge Insung Han for measuring the XRD pattern and Professor Shoemaker of UIUC for the use of the laboratory's diffractometer. This research used resources of the Advanced Photon Source, a U.S. Department of Energy (DOE) Office of Science User Facility operated for the DOE Office of Science by Argonne National Laboratory under contract no. DE-AC02-06CH11357. We thank George Sterbinsky, Tianpin Wu, and Steve Heald for the assistance during measurements at the APS. C.G. was supported by the Robert C. and Carolyn J. Springborn Endowment for Student Support Program and the National Science Foundation Graduate Research Fellowship Program. Any opinions, findings, and conclusions or recommendations expressed in this material are those of the author(s) and do not necessarily reflect the views of the National Science Foundation. This work was, in part, supported by a Packard Fellowship in Science and Engineering from the David and Lucile Packard Foundation. We thank Thomas Rossi and Michael Enright for fruitful discussion.

■ ABBREVIATIONS

QDs, quantum dots; CSQDs, core/shell QDs; UV/vis, UV/visible; PL, photoluminescence; XRD, X-ray diffraction; XPS, X-ray photoelectron spectroscopy; APT, atom probe tomography; XAS, X-ray absorption spectroscopy; EXAFS, extended X-ray absorption fine structure; TEM, transmission electron microscopy; SILAR, successive ion layer adsorption and reaction; CdO, cadmium oxide; OA, oleic acid; 1-ODE, 1-octadecene; TOP, trioctylphosphine; HDA, hexadecylamine; $ZnEt_2$, diethylzinc; TDPA, tetradecylphosphonic acid; HAADF, high annular dark-field; STEM, scanning transmission electron microscopy; HRTEM, high-resolution transmission electron microscopy; ICP-OES, inductively coupled plasma-optical emission spectrophotometry; APS, Advanced Photon Source; EDS, energy dispersive spectroscopy; XANES, X-ray absorption near-edge structure

■ REFERENCES

(1) Nozik, A. J.; Beard, M. C.; Luther, J. M.; Law, M.; Ellingson, R. J.; Johnson, J. C. Semiconductor Quantum Dots and Quantum Dot Arrays and Applications of Multiple Exciton Generation to Third-Generation Photovoltaic Solar Cells. *Chem. Rev.* **2010**, *110*, 6873−6890.

(2) Shirasaki, Y.; Supran, G. J.; Bawendi, M. G.; Bulović, V. Emergence of Colloidal Quantum-Dot Light-Emitting Technologies. *Nat. Photonics* **2013**, *7*, 13−23.

(3) Gao, X.; Cui, Y.; Levenson, R. M.; Chung, L. W. K.; Nie, S. In Vivo Cancer Targeting and Imaging with Semiconductor Quantum Dots. *Nat. Biotechnol.* **2004**, *22*, 969−976.

(4) Reiss, P.; Protière, M.; Li, L. Core/Shell Semiconductor Nanocrystals. *Small* **2009**, *5*, 154−168.

(5) Enright, M. J.; Cossairt, B. M. Synthesis of Tailor-Made Colloidal Semiconductor Heterostructures. *Chem. Commun.* **2018**, *54*, 7109−7122.

(6) Jiang, Y.; Cho, S.-Y.; Shim, M. Light-Emitting Diodes of Colloidal Quantum Dots and Nanorod Heterostructures for Future Emissive Displays. *J. Mater. Chem. C* **2018**, *6*, 2618−2634.

(7) Smith, A. M.; Nie, S. Semiconductor Nanocrystals: Structure, Properties, and Band Gap Engineering. *Acc. Chem. Res.* **2010**, *43*, 190−200.

(8) Jang, Y.; Shapiro, A.; Isarov, M.; Rubin-Brusilovski, A.; Safran, A.; Budniak, A. K.; Horani, F.; Dehnel, J.; Sashchiuk, A.; Lifshitz, E. Interface Control of Electronic and Optical Properties in IV−VI and II−VI Core/Shell Colloidal Quantum Dots: A Review. *Chem. Commun.* **2017**, *53*, 1002−1024.

(9) Chuang, C.-H. M.; Brown, P. R.; Bulović, V.; Bawendi, M. G. Improved Performance and Stability in Quantum Dot Solar Cells through Band Alignment Engineering. *Nat. Mater.* **2014**, *13*, 796−801.

(10) Zhu, H.; Yang, Y.; Wu, K.; Lian, T. Charge Transfer Dynamics from Photoexcited Semiconductor Quantum Dots. *Annu. Rev. Phys. Chem.* **2016**, *67*, 259−281.

(11) Nandan, Y.; Mehata, M. S. Wavefunction Engineering of Type-I/Type-II Excitons of CdSe/CdS Core-Shell Quantum Dots. *Sci. Rep.* **2019**, *9*, 2.

(12) Lambright, S.; Butaeva, E.; Razgoniaeva, N.; Hopkins, T.; Smith, B.; Perera, D.; Corbin, J.; Khon, E.; Thomas, R.; Moroz, P.; et al. Enhanced Lifetime of Excitons in Nonepitaxial Au/CdS Core/Shell Nanocrystals. *ACS Nano* **2014**, *8*, 352−361.

(13) McDaniel, H.; Pelton, M.; Oh, N.; Shim, M. Effects of Lattice Strain and Band Offset on Electron Transfer Rates in Type-II Nanorod Heterostructures. *J. Phys. Chem. Lett.* **2012**, *3*, 1094−1098.

(14) Bradshaw, L. R.; Knowles, K. E.; McDowall, S.; Gamelin, D. R. Nanocrystals for Luminescent Solar Concentrators. *Nano Lett.* **2015**, *15*, 1315−1323.

(15) Coropceanu, I.; Bawendi, M. G. Core/Shell Quantum Dot Based Luminescent Solar Concentrators with Reduced Reabsorption and Enhanced Efficiency. *Nano Lett.* **2014**, *14*, 4097−4101.

(16) Chen, C. Y.; Cheng, C. T.; Lai, C. W.; Hu, Y. H.; Chou, P. T.; Chou, Y. H.; Chiu, H. T. Type-II CdSe/CdTe/ZnTe (Core-Shell-Shell) Quantum Dots with Cascade Band Edges: The Separation of Electron (at CdSe) and Hole (at ZnTe) by the CdTe Layer. *Small* **2005**, *1*, 1215−1220.

(17) Chudzicki, M.; Werner, W. S. M.; Shard, A. G.; Wang, Y.-C.; Castner, D. G.; Powell, C. J. Evaluating the Internal Structure of Core-Shell Nanoparticles Using X-Ray Photoelectron Intensities and Simulated Spectra. *J. Phys. Chem. C* **2015**, *119*, 17687−17696.

(18) Chae, B. G.; Lee, J. H.; Park, S.; Lee, E.; Kwak, C. M.; Jafari, M.; Jeong, Y. K.; Park, C. G.; Seol, J. B. Direct Three-Dimensional Observation of Core/Shell-Structured Quantum Dots with a Composition-Competitive Gradient. *ACS Nano* **2018**, *12*, 12109−12117.

(19) Tedsree, K.; Li, T.; Jones, S.; Chan, C. W. A.; Yu, K. M. K.; Bagot, P. A. J.; Marquis, E. A.; Smith, G. D. W.; Tsang, S. C. E. Hydrogen Production from Formic Acid Decomposition at Room Temperature Using a Ag−Pd Core−Shell Nanocatalyst. *Nat. Nanotechnol.* **2011**, *6*, 302−307.

(20) Felfer, P.; Benndorf, P.; Masters, A.; Maschmeyer, T.; Cairney, J. M. Revealing the Distribution of the Atoms within Individual Bimetallic Catalyst Nanoparticles. *Angew. Chem., Int. Ed.* **2014**, *53*, 11190−11193.

(21) Felfer, P.; Li, T.; Eder, K.; Galinski, H.; Magyar, A. P.; Bell, D. C.; Smith, G. D. W.; Kruse, N.; Ringer, S. P.; Cairney, J. M. New Approaches to Nanoparticle Sample Fabrication for Atom Probe Tomography. *Ultramicroscopy* **2015**, *159*, 413−419.

(22) Jain, P. K.; Amirav, L.; Aloni, S.; Alivisatos, A. P. Nanoheterostructure Cation Exchange: Anionic Framework Conservation. *J. Am. Chem. Soc.* **2010**, *132*, 9997−9999.

(23) Shim, M. Colloidal Nanorod Heterostructures for Photovoltaics and Optoelectronics. *J. Phys. D: Appl. Phys.* **2017**, *50*, 173002.

(24) Maiti, S.; Ghorai, N.; Dana, J.; Ghosh, H. N. Disentangling the Electron and Hole Dynamics in Janus CdSe/PbSe Nanocrystals through Variable Pump Transient Absorption Spectroscopy. *J. Phys. Chem. C* **2018**, *122*, 29075−29079.

(25) McDaniel, H.; Zuo, J.-M.; Shim, M. Anisotropic Strain-Induced Curvature in Type-II CdSe/CdTe Nanorod Heterostructures. *J. Am. Chem. Soc.* **2010**, *132*, 3286−3288.

(26) Corrias, A.; Conca, E.; Cibin, G.; Mountjoy, G.; Gianolio, D.; De Donato, F.; Manna, L.; Casula, M. F. Insights into the Structure of Dot@Rod and Dot@Octapod CdSe@CdS Heterostructures. *J. Phys. Chem. C* **2015**, *119*, 16338−16348.

(27) Chen, L. Y.; Chen, C. H.; Tseng, C. H.; Lai, F. L.; Hwang, B. J. Synthesis $CdSe_xS_{1-x}$ Core/Shell Type Quantum Dots via One Injection Method. *Chem. Commun.* **2011**, *47*, 1592−1594.

(28) Godfrey, I. J.; Dent, A. J.; Parkin, I. P.; Maenosono, S.; Sankar, G. Structure of Gold−Silver Nanoparticles. *J. Phys. Chem. C* **2017**, *121*, 1957−1963.

(29) Bugaev, A. L.; Guda, A. A.; Lomachenko, K. A.; Shapovalov, V. V.; Lazzarini, A.; Vitillo, J. G.; Bugaev, L. A.; Groppo, E.; Pellegrini, R.; Soldatov, A. V.; et al. Core−Shell Structure of Palladium Hydride Nanoparticles Revealed by Combined X-Ray Absorption Spectroscopy and X-Ray Diffraction. *J. Phys. Chem. C* **2017**, *121*, 18202−18213.

(30) Wei, H.; Zhou, J.; Zhang, L.; Wang, F.; Wang, J.; Jin, C. The Core/Shell Structure of CdSe/ZnS Quantum Dots Characterized by X-Ray Absorption Fine Spectroscopy. *J. Nanomater.* **2015**, *2015*, 764712.

(31) Chen, L.-Y.; Yang, P.-A.; Tseng, C.-H.; Hwang, B.-J.; Chen, C.-H. Internal Structure of Tunable Ternary $CdSe_xS_{1-x}$ Quantum Dots Unraveled by X-Ray Absorption Spectroscopy. *Appl. Phys. Lett.* **2012**, *100*, 163113.

(32) Saha, A.; Shetty, A.; Pavan, A. R.; Chattopadhyay, S.; Shibata, T.; Viswanatha, R. Uniform Doping in Quantum-Dots-Based Dilute Magnetic Semiconductor. *J. Phys. Chem. Lett.* **2016**, *7*, 2420−2428.

https://dx.doi.org/10.1021/acs.jpcc.9b11443
J. Phys. Chem. C 2020, 124, 3895−3904

(33) Cho, D. Y.; Xi, L.; Boothroyd, C.; Kardynal, B.; Lam, Y. M. The Role of Ion Exchange in the Passivation of In(Zn)P Nanocrystals with ZnS. *Sci. Rep.* **2016**, *6*, 22818.
(34) Xie, R.; Zhong, X.; Basché, T. Synthesis, Characterization, and Spectroscopy of Type-II Core/Shell Semiconductor Nanocrystals with ZnTe Cores. *Adv. Mater.* **2005**, *17*, 2741−2745.
(35) Jiao, S.; Shen, Q.; Mora-Seró, I.; Wang, J.; Pan, Z.; Zhao, K.; Kuga, Y.; Zhong, X.; Bisquert, J. Band Engineering in Core/Shell ZnTe/CdSe for Photovoltage and Efficiency Enhancement in Exciplex Quantum Dot Sensitized Solar Cells. *ACS Nano* **2015**, *9*, 908−915.
(36) Jin, S.; Zhang, J.; Schaller, R. D.; Rajh, T.; Wiederrecht, G. P. Ultrafast Charge Separation from Highly Reductive ZnTe/CdSe Type II Quantum Dots. *J. Phys. Chem. Lett.* **2012**, *3*, 2052−2058.
(37) Jiang, Z.-J.; Kelley, D. F. Stranski−Krastanov Shell Growth in ZnTe/CdSe Core/Shell Nanocrystals. *J. Phys. Chem. C* **2013**, *117*, 6826−6834.
(38) Long, T.; Cao, J.; Jiang, Z.-J. Predictable Spectroscopic Properties of Type-II ZnTe/CdSe Nanocrystals and Electron/Hole Quenching. *Phys. Chem. Chem. Phys.* **2019**, *21*, 5824−5833.
(39) Groeneveld, E.; van Berkum, S.; van Schooneveld, M. M.; Gloter, A.; Meeldijk, J. D.; van den Heuvel, D. J.; Gerritsen, H. C.; de Mello Donega, C. Highly Luminescent (Zn,Cd)Te/CdSe Colloidal Heteronanowires with Tunable Electron−Hole Overlap. *Nano Lett.* **2012**, *12*, 749−757.
(40) Enright, M. J.; Sarsito, H.; Cossairt, B. M. Quantifying Cation Exchange of Cd^{2+} in ZnTe: A Challenge for Accessing Type II Heterostructures. *Chem. Mater.* **2017**, *29*, 666−672.
(41) Yang, P.; Wang, S.; Ando, M.; Murase, N. CdSe/Cd1−x Zn x S Core/Shell Quantum Dots with Tunable Emission: Growth and Morphology Evolution. *J. Mater. Sci.* **2013**, *48*, 651−658.
(42) Dorfs, D.; Franzl, T.; Osovsky, R.; Brumer, M.; Lifshitz, E.; Klar, T. A.; Eychmüller, A. Type-I and Type-II Nanoscale Heterostructures Based on CdTe Nanocrystals: A Comparative Study. *Small* **2008**, *4*, 1148−1152.
(43) *Reference X-ray Spectra of Metal Foils* http://exafsmaterials.com/Ref_Spectra_0.4MB.pdf (accessed Nov 30, 2019).
(44) Ravel, B.; Newville, M. ATHENA, ARTEMIS, HEPHAESTUS: Data Analysis for X-Ray Absorption Spectroscopy Using IFEFFIT. *J. Synchrotron Radiat.* **2005**, *12*, 537−541.
(45) Kasap, S.; Capper, P. Handbook of Electronic and Photonic Materials; Springer: 2007, *10*, 55.
(46) Jiang, Z.-J.; Kelley, D. F. Effects of Inhomogeneous Shell Thickness in the Charge Transfer Dynamics of ZnTe/CdSe Nanocrystals. *J. Phys. Chem. C* **2012**, *116*, 12958−12968.
(47) Kim, S.; Fisher, B.; Eisler, H.-J.; Bawendi, M. Type-II Quantum Dots: CdTe/CdSe(Core/Shell) and CdSe/ZnTe(Core/Shell) Heterostructures. *J. Am. Chem. Soc.* **2003**, *125*, 11466−11467.
(48) Rehr, J. J.; Kas, J. J.; Prange, M. P.; Sorini, A. P.; Takimoto, Y.; Vila, F. Ab Initio Theory and Calculations of X-Ray Spectra. *C. R. Phys.* **2009**, *10*, 548−559.
(49) Kisiel, A.; Robouch, B. V.; Marcelli, A. Local Crystalline Structure of Multinary Semiconducting Alloys: Random vs. Ordered Distributions. *Opto-Electron. Rev.* **2017**, *25*, 242−250.
(50) Groeneveld, E.; Witteman, L.; Lefferts, M.; Ke, X.; Bals, S.; Van Tendeloo, G.; De Mello Donega, C. Tailoring ZnSe-CdSe Colloidal Quantum Dots via Cation Exchange: From Core/Shell to Alloy Nanocrystals. *ACS Nano* **2013**, *7*, 7913−7930.
(51) De Trizio, L.; Manna, L. Forging Colloidal Nanostructures via Cation Exchange Reactions. *Chem. Rev.* **2016**, *116*, 10852−10887.
(52) Bailey, R. E.; Nie, S. Alloyed Semiconductor Quantum Dots: Tuning the Optical Properties without Changing the Particle Size. *J. Am. Chem. Soc.* **2003**, *125*, 7100−7106.
(53) Lee, S.; Flanagan, J. C.; Kim, J.; Yun, A. J.; Lee, B.; Shim, M.; Park, B. Efficient Type-II Heterojunction Nanorod Sensitized Solar Cells Realized by Controlled Synthesis of Core/Patchy-Shell Structure and CdS Cosensitization. *ACS Appl. Mater. Interfaces* **2019**, *11*, 19104−19114.
(54) Şahin, M.; Nizamoglu, S.; Yerli, O.; Volkan Demir, H. Reordering Orbitals of Semiconductor Multi-Shell Quantum Dot-Quantum Well Heteronanocrystals. *J. Appl. Phys.* **2012**, *111*, No. 023713.
(55) Smith, A. M.; Lane, L. A.; Nie, S. Mapping the Spatial Distribution of Charge Carriers in Quantum-Confined Heterostructures. *Nat. Commun.* **2014**, *5*, 4506.
(56) Jahrman, E. P.; Holden, W. M.; Ditter, A. S.; Mortensen, D. R.; Seidler, G. T.; Fister, T. T.; Kozimor, S. A.; Piper, L. F. J.; Rana, J.; Hyatt, N. C.; et al. An Improved Laboratory-Based X-Ray Absorption Fine Structure and X-Ray Emission Spectrometer for Analytical Applications in Materials Chemistry Research. *Rev. Sci. Instrum.* **2019**, *90*, No. 024106.

https://dx.doi.org/10.1021/acs.jpcc.9b11443
J. Phys. Chem. C 2020, 124, 3895−3904